forum acusticum 2026
8-12 September · Graz, Austria

ROLLAND: A NEW FRAMEWORK FOR REALISTIC AND COMPUTATIONALLY EFFICIENT ROLLING NOISE MODELING IN THE TIME DOMAIN

Maximilian Mantel[1], Ennes Sarradj[1]

[1] *Department of Engineering Acoustics, Institute of Fluid Dynamics and Technical Acoustics, Technische Universität Berlin, Einsteinufer 25, 10587 Berlin, Germany*

Abstract

Accurate simulation of noise generation and propagation during train pass-bys remains a persistent challenge in railway acoustics. Most current rolling noise models are forced into a compromise, suffering from either oversimplified assumptions or expensive computational demands. To address this, the present work introduces the fundamental framework for ROLLAND, a novel time-domain model. By applying an explicit finite difference scheme, the approach achieves detailed simulations while maintaining exceptional computational efficiency. The developed time-domain approach allows for the integration of spatially varying track properties and the implementation of multiple, truly moving sound sources. This provides a comprehensive basis for simulating realistic train pass-bys on tracks. At its core, the model utilizes Timoshenko beam theory to characterize bending wave propagation. Moving beyond the limitations of conventional models that often isolate vertical dynamics, ROLLAND also integrates lateral bending, torsional waves, and rail warping, thereby capturing the complex behavior of coupled waves. The framework also accounts for eccentricities in both rail head excitation and rail foot support. In this initial phase, the study focuses on a continuous slab track, modeled as an infinite structure through the application of complex-frequency-shifted perfectly matched layers (CFS-PML). Initial results, focused on the track's impulse response under vertical and lateral loads, demonstrate excellent agreement with an analytical reference model.

Keywords: *Rail vibration, Coupled wave propagation, Time domain, Finite difference method, Perfectly matched layer*

Corresponding author: *maximilian.mantel@tu-berlin.de.*

Introduction

Rolling noise is the dominant noise source in rail transport across a broad speed range [1]. It arises from complex mechanical interactions between wheel and track dynamics, driven by surface roughness and vehicle motion. Despite significant progress in acoustic modeling, established rolling noise models often account for only a subset of these sound generation mechanisms [2]. These limitations typically arise from simplified track geometries, idealized contact models, or the omission of multi-wheel interactions.

A major physical complexity in rolling noise generation arises from coupled wave propagation along the rail. Wheel–rail contact transmits both vertical and lateral force components at the rail head (Fig. 1). Because this excitation acts eccentrically relative to the rail center of gravity, and because the rail profile itself is asymmetric, the contact forces excite coupled vertical bending, lateral bending, and torsional waves. Furthermore, the elastic support reaction at the rail foot, acting at an eccentricity z_{f}, further couples these wave types.

To address these physical complexities in a computationally efficient manner, we present ROLLAND[1], an open-source time-domain simulation framework based on an explicit finite-difference method (FDM), and detail its mathematical foundation. The proposed model represents the rail as a discrete 1D beam with seven degrees of freedom (DOFs) per node at the rail center of gravity. The framework explicitly incorporates all mechanical eccentricities shown in Fig. 1. It thereby simulates the coupled propagation of vertical, lateral, and torsional waves as well as cross-sectional warping under continuous elastic rail pad support. Although the modular architecture of ROLLAND readily extends to discrete two-layer track systems (e.g., ballasted tracks with sleepers), this work establishes the foundational mathematical formulation applied to a

[1] `https://github.com/mantelmax/rolland`

continuous single-layer slab track.
While the mechanical formulation builds on the framework proposed by [3], the core novelty of this work lies in its numerical time-domain strategy, extending earlier beam-on-foundation models [4]. Specifically, the main contributions are:

1. The time-domain implementation of a coupled multi-DOF rail model that solves 21 coupled differential equations using an explicit finite-difference method.
2. A complex frequency-shifted perfectly matched layer (CFS-PML) boundary treatment to accurately simulate infinite railway tracks.
3. A flexible formulation capable of simulating moving excitations over non-periodic support conditions, allowing the track composition to be defined arbitrarily along the rail.

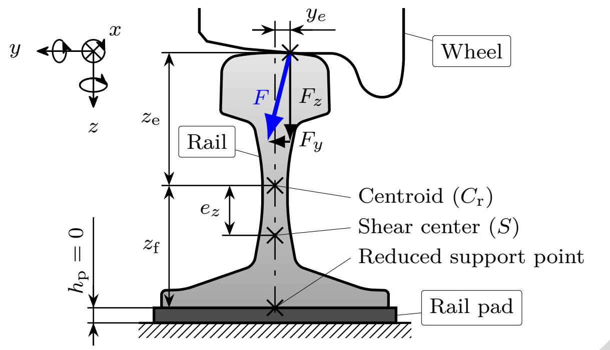

Figure 1: Eccentricities of mechanical properties relative to the rail centroid in a single-layer rail model (adapted from [3]).

Rail model

The mechanical rail formulation is based on the semi-analytical model proposed by [3], [5], which governs the coupled propagation of longitudinal, bending, and torsional waves, as well as cross-sectional warping along a one-dimensional beam. The governing system of partial differential equations is expressed as

$$
\begin{aligned}
(\mathbf{K}_{\text{fnd}} + \mathbf{K}_0)\mathbf{U} + \mathbf{K}_1 \frac{\partial \mathbf{U}}{\partial x} + \mathbf{K}_2 \frac{\partial^2 \mathbf{U}}{\partial x^2} \\
+ \mathbf{D}\frac{\partial \mathbf{U}}{\partial t} + \mathbf{M}\frac{\partial^2 \mathbf{U}}{\partial t^2} = \mathbf{F},
\end{aligned}
\tag{1}
$$

where $\mathbf{K}_{\text{fnd}}$ represents all mechanical properties of the superstructure (Fig. 2) acting at the rail centroid. $\mathbf{K}_0, \mathbf{K}_1$, and $\mathbf{K}_2$ represent the rail stiffness matrices, $\mathbf{D}$ is the global viscous damping matrix, $\mathbf{M}$ is the mass matrix, and $\mathbf{F}$ the external excitation vector. The state vector $\mathbf{U} = [u_x, u_z, u_y, \phi_x, \phi_z, \phi_y, u_{\text{w}}]^{\text{T}}$ groups the translational and rotational DOFs defined at the rail centroid.
Two main modifications are made relative to the formulation in [3]:

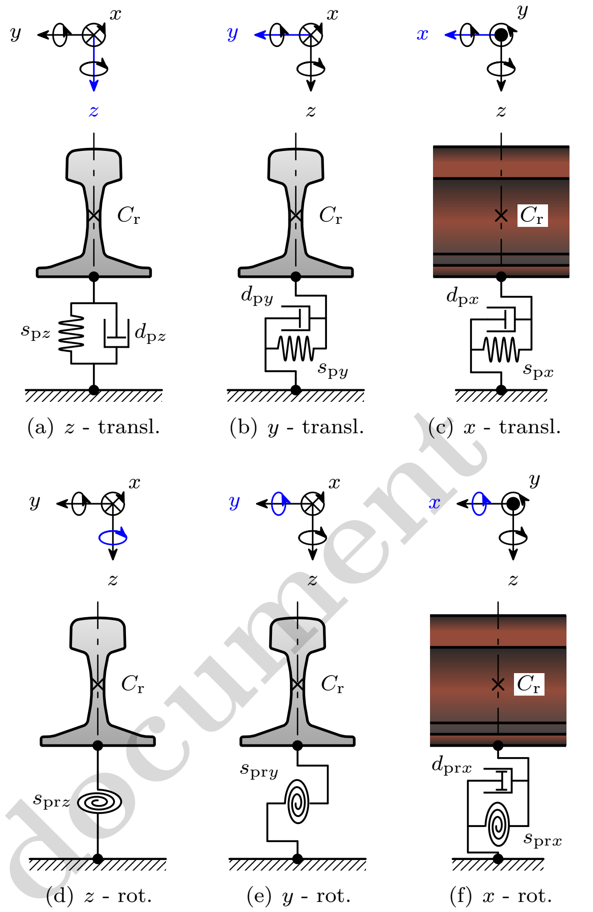

Figure 2: Overview of the overall mechanical system. Each view shows the mechanical properties of a single DOF. The pad stiffness against rail warping is not shown.

1. The hysteretic damping model is replaced with an equivalent viscous damping formulation to facilitate explicit time-domain simulation.
2. The warping coupling terms within the bending wave equations are omitted. These terms induce numerical instability but have negligible influence on the rail impulse response.

The global viscous damping matrix $\mathbf{D}$ combines the foundation damping $\mathbf{D}_{\text{fnd}}$ (transformed to the rail centroid) and the internal rail damping $\mathbf{D}_{\text{r}}$:

$$
\mathbf{D} = \mathbf{D}_{\text{fnd}} + \mathbf{D}_{\text{r}} = \mathbf{T}_{\text{f}}^{\text{T}} \mathbf{D}_{\text{p}} \mathbf{T}_{\text{f}} + \mathbf{D}_{\text{r}}. \tag{2}
$$

The transformation matrix $\mathbf{T}_{\text{f}}$ maps the elastic and dissipative properties from the rail foot to the centroid [3]. At the rail foot, pad damping is applied exclusively to translational DOFs and axial torsion (Fig. 2) through the diagonal matrix:

$$
\mathbf{D}_{\text{p}} = \text{diag}(d_{\text{p}x}, d_{\text{p}z}, d_{\text{p}y}, d_{\text{pr}x}, 0, 0, 0). \tag{3}
$$

To approximate hysteretic damping behavior across a broad frequency range, each viscous damping coefficient $d_{\mathrm{p},j}$ is calibrated using

$$d_{\mathrm{p},j} = \frac{\eta_\mathrm{p} s_{\mathrm{p},j}}{\omega_j}, \tag{4}$$

where η_p is the pad loss factor, $s_{\mathrm{p},j}$ is the pad stiffness for the given DOF, and ω_j is a characteristic tuning frequency. These damping coefficients are tuned to the first cut-on frequencies of the coupled longitudinal, vertical, lateral, and torsional waves. These frequencies can be determined by

$$\left|(\mathbf{K}_\mathrm{fnd} + \mathbf{K}_0) - \omega^2 \mathbf{M}\right| = 0. \tag{5}$$

This condition defines the threshold for free wave propagation in the frequency domain, where the positive roots ω_j of Eq. (5) form the set of reference frequencies $\Omega_\mathrm{d} = \{\omega_x, \omega_z, \dots\}$ used for the respective viscous damping coefficients [1]. While longitudinal and vertical damping coefficients depend on their respective pad stiffnesses and cut-on frequencies, coupled lateral–torsional waves require cross-assigned cut-on frequencies. To prevent the frequency-dependent lateral viscous damping from over-damping higher-frequency torsion, lateral damping uses the torsional cut-on frequency and vice versa. In contrast to pad damping, internal rail damping $\mathbf{D}_\mathrm{r}$ acts directly at the centroid with minor magnitude relative to pad damping.

Boundary domain

To simulate an infinite track without wave reflections, a CFS-PML boundary is implemented in the time domain. Wave absorption within the boundary layer is governed by the complex coordinate stretching function [6]

$$\lambda = \frac{\partial \overline{x}}{\partial x} = 1 + \frac{\sigma}{\mathrm{i}\omega + \alpha}, \tag{6}$$

where α denotes the frequency-shifting coefficient and σ is the spatial damping profile (Fig. 3) defined by

$$\sigma(x) = \begin{cases} a\left(\frac{\max(x_\mathrm{l}-x,\, x-x_\mathrm{r})}{l_\mathrm{bd}}\right)^m & : x \notin [x_\mathrm{l}, x_\mathrm{r}] \\ 0 & : x \in [x_\mathrm{l}, x_\mathrm{r}] \end{cases} \tag{7}$$

containing the maximum PML coefficient a, the boundary length l_bd and the exponent m. Applying the inverse stretching function to the spatial derivatives yields the modified differential operators:

$$\frac{\partial \mathbf{U}_\mathrm{bd}}{\partial \overline{x}} = \frac{\partial \mathbf{U}}{\partial x} - \sigma \underbrace{\frac{1}{\mathrm{i}\omega + \sigma + \alpha} \frac{\partial \mathbf{U}}{\partial x}}_{\boldsymbol{\psi}}, \tag{8}$$

$$\begin{aligned} \frac{\partial^2 \mathbf{U}_\mathrm{bd}}{\partial \overline{x}^2} = {} & \frac{\partial}{\partial x}\left(\frac{\partial \mathbf{U}}{\partial x} - \sigma \boldsymbol{\psi}\right) \\ & - \sigma \underbrace{\frac{1}{\mathrm{i}\omega + \sigma + \alpha} \frac{\partial}{\partial x}\left(\frac{\partial \mathbf{U}}{\partial x} - \sigma \boldsymbol{\psi}\right)}_{\boldsymbol{\theta}}. \end{aligned} \tag{9}$$

To evaluate these expressions in the time domain, an Auxiliary Differential Equation (ADE) formulation is adopted [7]. The frequency-dependent terms are represented by auxiliary vectors $\boldsymbol{\psi}$ and $\boldsymbol{\theta}$, each containing one auxiliary variable per DOF. Transforming back to the time domain yields the governing ADE systems:

$$\frac{\partial \boldsymbol{\psi}}{\partial t} = \frac{\partial \mathbf{U}}{\partial x} - (\sigma + \alpha)\boldsymbol{\psi}, \tag{10}$$

$$\frac{\partial \boldsymbol{\theta}}{\partial t} = \frac{\partial}{\partial x}\left(\frac{\partial \mathbf{U}}{\partial x} - \sigma \boldsymbol{\psi}\right) - (\sigma + \alpha)\boldsymbol{\theta}. \tag{11}$$

Substituting the first and second spatial derivatives of the state vector $\mathbf{U}$ according to Eqs. (8) and (9) yields the final system of equations:

$$\begin{aligned} (\mathbf{K}_\mathrm{fnd} + \mathbf{K}_0)\mathbf{U} + \mathbf{K}_1 \frac{\partial \mathbf{U}_\mathrm{bd}}{\partial \overline{x}} + \mathbf{K}_2 \frac{\partial^2 \mathbf{U}_\mathrm{bd}}{\partial \overline{x}^2} & \\ + \mathbf{D}\frac{\partial \mathbf{U}}{\partial t} + \mathbf{M}\frac{\partial^2 \mathbf{U}}{\partial t^2} & = \mathbf{F}. \end{aligned} \tag{12}$$

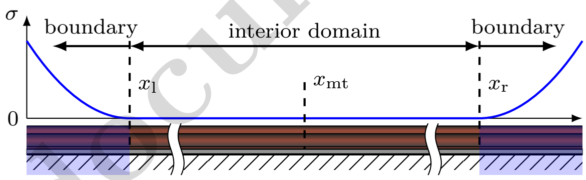

Figure 3: Division of the calculation domain into an interior domain and two boundary domains using the corresponding damping profile $\sigma(x)$. The positions x_l and x_r indicate the transitions, while x_mt denotes the mid-track position.

Discretization and Solution

The governing system, comprising the seven primary wave equations (Eq. (12)) and 14 boundary ADEs (Eqs. (10)–(11)), is solved in the time domain using an explicit finite difference scheme implemented in Devito [8], [9]. The continuous spatial-temporal domain is discretized on a uniform grid with spatial step Δx and time step Δt, defined by $x_i = i\,\Delta x$ and $t^n = n\,\Delta t$, yielding state samples $\mathbf{U}_i^n \approx \mathbf{U}(x_i, t^n)$.
Spatial derivatives of the primary state vector $\mathbf{U}$ are discretized using 6th-order central finite difference stencils:

$$\left.\frac{\partial \mathbf{U}}{\partial x}\right|_i^n \approx \frac{1}{60\,\Delta x} \sum_{k=1}^{3} c_k \left(\mathbf{U}_{i+k}^n - \mathbf{U}_{i-k}^n\right), \tag{13}$$

$$\text{with } (c_1, c_2, c_3) = (45, -9, 1),$$

$$\left.\frac{\partial^2 \mathbf{U}}{\partial x^2}\right|_i^n \approx \frac{1}{\Delta x^2}\left[-\frac{49}{18}\mathbf{U}_i^n + \sum_{k=1}^{3} b_k \left(\mathbf{U}_{i+k}^n + \mathbf{U}_{i-k}^n\right)\right], \tag{14}$$

$$\text{with } (b_1, b_2, b_3) = \left(\tfrac{3}{2}, -\tfrac{3}{20}, \tfrac{1}{90}\right).$$

For the auxiliary vector $\boldsymbol{\psi}$, spatial derivatives are approximated using a 2nd-order central scheme:

$$\left.\frac{\partial \psi}{\partial x}\right|_i^n \approx \frac{\psi_{i+1}^n - \psi_{i-1}^n}{2\,\Delta x}. \tag{15}$$

Because Devito solves the resulting differential equations from Eq. (12) sequentially within each time step, temporal stencil selection depends directly on the evaluation sequence. Primary state variables (DOFs) that have not yet been updated in the current sequence—denoted here as $\mathbf{U}_{\mathrm{bw}}$—are discretized using backward temporal stencils ($s = 0$). Conversely, terms involving the active DOF currently being solved or DOFs already updated in preceding equations—denoted as $\mathbf{U}_{\mathrm{fw}}$—are discretized using forward temporal stencils ($s = 1$). Temporal derivatives of the auxiliary variables $(\boldsymbol{\theta}, \boldsymbol{\psi})$ require only 1st-order forward stencils ($s = 1$), as their governing equations contain no time derivatives of other fields.
The temporal derivative operators [10] are unified via the shift parameter $s \in \{0, 1\}$:

$$\left.\frac{\partial \mathbf{Q}}{\partial t}\right|_i^n \approx \frac{\mathbf{Q}_i^{n+s} - \mathbf{Q}_i^{n+s-1}}{\Delta t}, \tag{16}$$

$$\left.\frac{\partial^2 \mathbf{W}}{\partial t^2}\right|_i^n \approx \frac{\mathbf{W}_i^{n+s} - 2\mathbf{W}_i^{n+s-1} + \mathbf{W}_i^{n+s-2}}{\Delta t^2}, \tag{17}$$

where 1^{st}-order time derivatives (16) apply to all fields $\mathbf{Q} \in \{\mathbf{U}_{\mathrm{fw}}, \mathbf{U}_{\mathrm{bw}}, \boldsymbol{\theta}, \boldsymbol{\psi}\}$, while 2^{nd}-order time derivatives (17) apply exclusively to the primary wave fields $\mathbf{W} \in \{\mathbf{U}_{\mathrm{fw}}, \mathbf{U}_{\mathrm{bw}}\}$.

Stability analysis

For explicit finite difference schemes, numerical stability is governed by the Courant–Friedrichs–Lewy (CFL) condition [11], which requires that the numerical propagation speed does not exceed the physical wave speed. For the present beam formulation, the Courant number C is defined as

$$C = c_{\mathrm{L}} \frac{\Delta t}{\Delta x} = \sqrt{\frac{E}{\rho}} \frac{\Delta t}{\Delta x} \le C_{\max} \le 1, \tag{18}$$

where $c_{\mathrm{L}} = \sqrt{E/\rho}$ is the longitudinal wave speed in the rail, representing the maximum phase velocity in the system.
The stability and accuracy of the numerical scheme is evaluated through a grid convergence study varying the temporal step size Δt and spatial step size Δx, using pad properties from Tab. 1 and rail parameters from [3]. Broadband excitation is applied independently in the vertical and lateral directions at positions Pos. 1 and Pos. 2 (Fig. 6) using a Gaussian impulse according to [4]. To quantify numerical accuracy, the error metric

$$\varepsilon = \frac{1}{\ln(f_{\max}/f_{\min})} \int_{f_{\min}}^{f_{\max}} \frac{\left||\underline{Y}_{\mathrm{ref}}(f)| - |\underline{Y}(f)|\right|}{|\underline{Y}_{\mathrm{ref}}(f)|} \frac{\mathrm{d}f}{f} \tag{19}$$

is defined as the mean deviation of the point mobility $\underline{Y} = \underline{v}/\underline{F}$ (ratio of complex velocity response to excitation force) from a reference simulation $\underline{Y}_{\mathrm{ref}}$ computed on the finest grid across the frequency range from 50 Hz to 6000 Hz. As shown in Fig. 4, $C_{\max}$ decreases as the spatial step size increases; nevertheless, the scheme remains numerically stable across a wide parameter range and exhibits minimal discretization errors even on coarser grids.

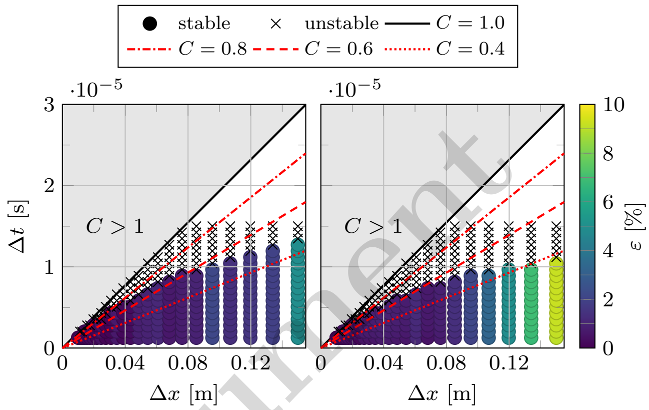

Figure 4: Stability analysis for different grid resolutions: vertical excitation at Pos. 1 (left) and lateral excitation at Pos. 2 (right). The error metric is calculated by Eq. (19).

In parallel, a parametric sensitivity analysis of the CFS-PML boundary domain is performed for two spatial step sizes by varying the number of boundary layers n_{b} and the frequency-shifting coefficient α (Fig. 5). To excite all coupled wave types, lateral excitation is applied directly at the computational–boundary domain interface. The previous error metric (Eq (19)) is used again. A simulation with conservative boundary parameters ($n_{\mathrm{b}} = 800$, $\alpha = 0$) serves as the reference solution. The stability of the boundary layer depends primarily on its total length, with stable configurations yielding consistently low reflection errors. Notably, increasing the frequency-shifting coefficient α substantially reduces the minimum boundary layer length without sacrificing stability.

Validation

The proposed numerical model is validated using the rail pad and simulation parameters listed in Tabs. 1 and 2, alongside the rail cross-sectional properties from [3]. The spatial and temporal discretization (0.05 m and 0.5×10^{-5} s) provides a stable solution and an optimal balance between accuracy and computational efficiency (Fig. 4). Under these conditions, a 0.5 s time-domain simulation requires approximately 7 s of execution time on an Intel® Core™ i5-1340P CPU (16 threads).
Model accuracy is evaluated by computing point and transfer mobilities under vertical excitation at Pos. 1 and lateral excitation at Pos. 2 (Fig. 6). Excitation is applied at the track center, and transfer mobilities are evaluated at a distance of 10 m. The FDM predictions are benchmarked against impulse responses

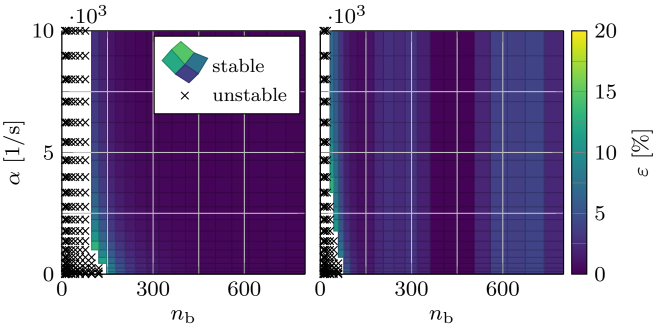

Figure 5: Boundary stability analysis for a dense (left, $\Delta x = 0.025\,\mathrm{m}$, $\Delta t = 3 \times 10^{-6}\,\mathrm{s}$) and a coarse grid (right, $\Delta x = 0.1\,\mathrm{m}$, $\Delta t = 7 \times 10^{-6}\,\mathrm{s}$). The error is evaluated according to Eq. (19) by the mean point mobility deviation of test simulations excited at the boundary domain transition x_{l} (Fig. 3), relative to a conservative reference simulation ($\alpha = 0$, $n_{\mathrm{b}} = 800$) with mid-track excitation.

from the semi-analytical model [3], comparing both the original hysteretic damping formulation and the proposed equivalent viscous damping model.

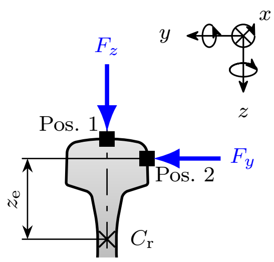

Figure 6: Excitation positions on the rail head profile: vertical excitation at Pos. 1 and lateral excitation at Pos. 2.

As shown in Fig. 7, the FDM model and the semi-analytical model with equivalent viscous damping show excellent agreement across all computed mobility curves. Relative to the reference hysteretic model, the viscous formulation introduces slight overdamping in specific frequency regimes. Specifically, this attenuation affects the torsional resonance in the point mobility at Pos. 2 (around 350 Hz) and the vertical transfer mobility at Pos. 1 above 300 Hz.
Finally, the boundary absorption performance is evaluated across four excitation scenarios: applying excitation either at the track center (x_{mt}) or directly at the boundary interface (x_{l}), with the CFS-PML layers either active or disabled (Fig. 8). Without PML absorption, non-physical boundary reflections severely distort the solution, even for mid-track excitation far from the domain boundary. Activating the CFS-PML layer suppresses these reflections almost completely, restoring the dynamic response of an infinite track regardless of the excitation location.

Conclusions

This work introduces the mathematical and numerical foundation of ROLLAND, an open-source time-domain

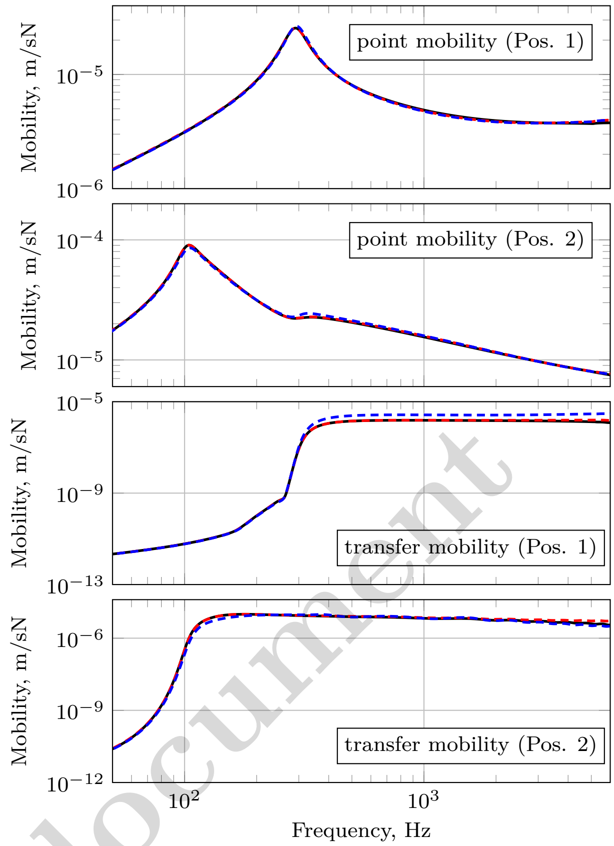

Figure 7: Impulse responses under vertical (Pos. 1) and lateral (Pos. 2) track-center excitation (transfer mobility evaluated at 10 m). Comparison between the numerical model (—) and the semi-analytical model [3] using viscous (- - -) and hysteretic damping (- - -).

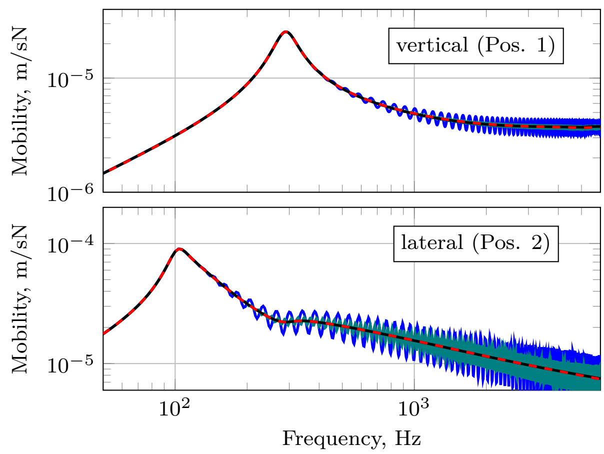

Figure 8: Evaluation of CFS-PML boundary absorption across four excitation scenarios: boundary interface excitation without PML (—), mid-track excitation at x_{mt} without PML (—), boundary interface excitation at x_{l} with PML (- - -), and mid-track excitation at x_{mt} with PML (—).

framework for rolling noise simulations. By modeling the rail as a discrete 1D beam with seven degrees of

Table 1: Rail pad properties. Stiffness values are given per unit length. Rotational parameters are calculated according to [12].

Parameter	Value	Unit
Long. stiffness, s_{px}	67×10^6	$\mathrm{N\,m^{-2}}$
Vertical stiffness, s_{pz}	200×10^6	$\mathrm{N\,m^{-2}}$
Lateral stiffness, s_{py}	67×10^6	$\mathrm{N\,m^{-2}}$
Loss factor, η_p	0.2	—
Rail pad length, l_p	0.15	m
Rail pad height, h_p	0	m

Table 2: Numerical simulation parameters.

Parameter	Value	Unit
Simulation time, t_{end}	0.5	s
Spatial step size, Δx	0.05	m
Temporal step size, Δt	0.5×10^{-5}	s
Track length, l_{track}	60	m
PML layers, n_b	200	—
Damping exponent, m	3	—
Frequency-shifting coefficient, α	10 000	$\mathrm{s^{-1}}$
Max. PML coefficient, a	1×10^5	$\mathrm{s^{-1}}$

freedom per node, the framework explicitly captures coupled vertical, lateral, and torsional wave propagation as well as cross-sectional warping under eccentric excitation and foot support. Implemented via an explicit finite-difference scheme in Devito, the solver achieves high computational efficiency, running a 0.5 s simulation in approximately 7 s on a standard desktop CPU.

The model is validated against a semi-analytical benchmark across a broad frequency range from 50 Hz to 6000 Hz. The proposed equivalent viscous damping formulation demonstrates good overall agreement with the reference hysteretic model, though slight overdamping occurs near the torsional resonance (around 350 Hz) and in the vertical transfer mobility above 300 Hz. Furthermore, the integrated CFS-PML boundary effectively eliminates artificial boundary reflections, accurately reproducing infinite-track dynamics even when excitation is applied directly at the boundary interface.

While the present formulation establishes the core framework for a continuous single-layer slab track, its time-domain formulation lays the groundwork for simulating scenarios beyond the reach of conventional frequency-domain models. Future work extends ROLLAND to support discrete ballasted tracks with excitation from multiple moving wheels under non-linear Hertzian contact dynamics.

References

[1] D. Thompson, *Railway Noise and Vibration: Mechanisms, Modelling and Means of Control*. Elsevier, Dec. 2008. DOI: 10.1016/B978-0-08-045147-3.X0023-0

[2] A. C. Lamprea-Pineda, D. P. Connolly, and M. F. Hussein, “Beams on elastic foundations – a review of railway applications and solutions,” *Transportation Geotechnics*, vol. 33, p. 100 696, Mar. 2022. DOI: 10.1016/j.trgeo.2021.100696

[3] D. Kostovasilis, D. Thompson, and M. Hussein, “A semi-analytical beam model for the vibration of railway tracks,” *Journal of Sound and Vibration*, vol. 393, pp. 321–337, Apr. 2017. DOI: 10.1016/j.jsv.2016.12.033

[4] K. Stampka and E. Sarradj, “A time-domain finite-difference method for bending waves on infinite beams on an elastic foundation,” *Acoustics*, vol. 4, pp. 867–884, Jan. 1, 2022. DOI: 10.3390/acoustics4040052

[5] D. Kostovasilis, “Analytical modelling of the vibration of railway track,” Doctoral dissertation, University of Southampton, 2017.

[6] M. Kuzuoglu and R. Mittra, “Frequency dependence of the constitutive parameters of causal perfectly matched anisotropic absorbers,” *IEEE Microwave and Guided Wave Letters*, vol. 6, no. 12, pp. 447–449, Dec. 1996. DOI: 10.1109/75.544545

[7] S. D. Gedney and B. Zhao, “An auxiliary differential equation formulation for the complex-frequency shifted PML,” *IEEE Transactions on Antennas and Propagation*, vol. 58, no. 3, pp. 838–847, Mar. 2010. DOI: 10.1109/TAP.2009.2037765

[8] M. Louboutin et al., “Devito (v3.1.0): An embedded domain-specific language for finite differences and geophysical exploration,” *Geoscientific Model Development*, vol. 12, no. 3, pp. 1165–1187, 2019. DOI: 10.5194/gmd-12-1165-2019

[9] F. Luporini et al., “Architecture and performance of devito, a system for automated stencil computation,” *ACM Trans. Math. Softw.*, vol. 46, no. 1, Apr. 2020, ISSN: 0098-3500. DOI: 10.1145/3374916

[10] R. J. LeVeque, *Finite Difference Methods for Ordinary and Partial Differential Equations: Steady-State and Time-Dependent Problems*. Society for Industrial and Applied Mathematics, Jan. 2007. DOI: 10.1137/1.9780898717839

[11] R. Courant, K. Friedrichs, and H. Lewy, “Über die partiellen Differenzengleichungen der mathematischen Physik,” *Mathematische Annalen*, vol. 100, no. 1, pp. 32–74, Dec. 1, 1928. DOI: 10.1007/BF01448839

[12] D. Thompson, W. Van Vliet, and J. Verheij, “Developments of the indirect method for measuring the high frequency dynamic stiffness of resilient elements,” *Journal of Sound and Vibration*, vol. 213, no. 1, pp. 169–188, May 1998. DOI: 10.1006/jsvi.1998.1492